

5 **Structural variability within the Kane oceanic core complex from full waveform
 inversion and reverse time migration of streamer data**

 Min Xu^{1, 2, 3, *}, Xu Zhao^{1, 2, 3, 4}, J. Pablo Canales⁵

¹CAS Key Laboratory of Ocean and Marginal Sea Geology, South China Sea Institute of
Oceanology, Guangzhou, China

10 ²Innovation Academy of South China Sea Ecology and Environmental Engineering,
Chinese Academy of Sciences, Guangzhou, China

³Southern Marine Science and Engineering Guangdong Laboratory, Guangzhou, China

⁴University of Chinese Academy of Sciences, Beijing, China

⁵Department of Geology and Geophysics, Woods Hole Oceanographic Institution, Woods
Hole, MA, USA

15

Contents of this file

 Text S1 to S3

 Figures S1 to S12

Introduction

20 This supporting information file presents seismic data and preprocessing ([Text S1](#),
[Figures S1-S2](#)), methods of early-arrival full waveform inversion (FWI, [Text S2](#), [Figures
S3-S10](#)) and reverse time migration (RTM, [Text S3](#), [Figures S11-S12](#)) and execution
processes employed in this study.

Text S1. Seismic data and preprocessing

25 The multi-channel seismic (MCS) data used in this study were acquired in 2001
onboard the seismic *R/V* Maurice Ewing (cruise EW0102) using a 6-km-long, 480-
channel hydrophone streamer towed at a nominal depth of 10 m. A tuned 10-element air

gun array with a total volume of 3,100 cubic inches, deployed at a nominal depth of 8 m, was used as the seismic source. The shot and group spacing was 37.5 m and 12.5 m, respectively, and the data recording length was 10 s with a sampling rate of 4 ms. The distance between the air gun array and the closest channel was ~200 m. The MCS data employed in this study include three dip profiles (K4, K1, K8) and three strike profiles (K5, K6, K7) at the Kane oceanic core complex (OCC). These profiles cover and sample the main morphological features of the Kane OCC, i.e., cross each of the corrugated surfaces along dip and strike directions. The dip profiles extend to the east across the fossil hanging wall remnant, strike profiles K1 and K4 extend westward across the breakaway zone.

The long shot-receiver offsets and relatively shallow seafloor depths across the Kane OCC allowed us to record clear subseafloor refractions (Figure S1) that we used in early-arrival FWI. Seismic data preconditioning strategies were applied in order to increase the convergence rate for the FWI iterative scheme and reduce the risk of converging to local minima. Data preprocessing consisted of trace editing to exclude bad shots/channels, interpolating noisy traces, surface-consistent amplitude balancing, and bandpass filtering (1-6-100-125 Hz) to denoise the data. We also applied a despiking processing flow based on the LIFT techniques developed by Choo *et al.* (2004) to enhance signal-to-noise ratio and suppress high-amplitude spikes that can lead to smearing during migration, while preserving amplitude integrity.

The LIFT processing procedure was similar to those described in Aghaei *et al.* (2014) and Han *et al.* (2016). First, the data were band-pass filtered (1-6-100-125 Hz) and separated into three frequency bands: low-pass filtered (15-20 Hz), high-pass filtered (20-25 Hz), and intermediate band by subtracting the low and high frequency components from the raw data. We call these LB, IB, and HB for the low, intermediate, and high-frequency bands, respectively. LB was despiked in the time-frequency domain by scaling spectral amplitudes of each trace that exceeded a pre-determined threshold above the median spectral amplitude of nearby traces. After despiking, we applied a frequency-wavenumber (f-k) filter to LB, resulting in a cleaned low-frequency band (LBC). Cleaning of IB consisted of two-pass despiking, without f-k filtering: a first despiking pass (as described above for LB), resulting in IBC1, and a second pass in which the noise removed after the first pass (i.e., IB-IBC1) was further cleaned to isolate any residual seismic signal that may have eliminated during the first despiking pass. This residual signal (IBC2) was added back to the first-pass cleaned IBC1, resulting in a cleaned intermediate band (IBC). The high-frequency band HC was processed as the intermediate band, resulting in a cleaned high-frequency band (HBC). The LIFT process was completed by adding the three cleaned bands (LBC+IBC+HBC) to form a clean shot gather (Figure S2).

Prior to FWI and RTM, the geometrical spreading through a 3D medium was accounted for by transforming the real 3D data into approximate 2D data by multiplying by $t^{1/2}$ (where t is the two-way travelttime), which transforms spherical geometric spreading into a cylindrical geometrical spreading mode. The preprocessed data were bandpass filtered with 6-8-10-15 Hz and 6-8-15-20 Hz for two-step FWI runs. The shot gathers were then windowed in the time-offset domain by applying a 1.8-s-wide time

75 window located 0.2 s above the seafloor reflections in the 160 far-offset traces (4,182-6,182 m source-receiver offsets, [Figure S1](#)). The windowing allows FWI only focusing on the early refraction arrivals, and excluding energy from seafloor reflections, scattering, and direct water arrivals.

Text S2. Early-arrival full waveform inversion

80 FWI refers to a collection of techniques that use the information from the traveltimes and waveform shapes of seismic data to derive high-fidelity earth models for seismic imaging. The inversion algorithm was originally developed by *Lailly (1983)* and *Tarantola (1984)* through recasting the migration imaging principle of *Claerbout (1971)* as a local optimization problem, the aim of which is least-squares minimization of the misfit between recorded and modeled wavefield data. Since these pioneering efforts substantial research has been conducted to implement FWI in both the time and frequency domains (e.g., *Pratt, 1999*; *Sirgue & Pratt, 2004*; *Operto et al., 2007*; *Vigh & Starr, 2008*).

90 The acoustic FWI employed in this study targets the energy corresponding to the early-arrival refraction events, which are basically compressional waves. The forward modeling of the full wavefield and back propagation of the residual wavefield are calculated in the time domain using a fourth order in space, second order in time finite difference scheme (*Levander, 1988*). The misfit function is minimized iteratively by computing the gradient (*Tarantola, 1984*) of successive updated models. It uses the gradient for estimating an initial direction and updating it using the Polak-Ribière implementation of the conjugate gradient method (*Grippo & Lucidi, 1997*). The line search along the directions uses the BB formula (*Barzilai & Borwein, 1988*) for an initial step-length, and then applies the backtracking line-search method to update it. The inversion problem is highly nonlinear and has many spurious local minima. Successful conduct of FWI on MCS data requires low-frequency, far-offset data, as well as a relatively precise source wavelet and starting model that contains the long and possibly the intermediate wavelengths of the true velocity model.

100 The starting velocity models were the traveltome tomography models of *Xu et al. (2009)*. As the first arrivals have limited depth coverage, we extrapolated traveltome tomography models to the whole model domain, and then used the result as starting models for FWI in order to make sure that we have some constraints below turning rays. The grid spacing used in finite-difference forward modeling is 15 m and 9.375 m. The initial waveform forward modeling showed that the traveltome tomography models can accurately predict first arrival travetomes within ~20 ms ([Figure S6](#)). Time domain implementation of FWI usually suffers from cycle-skipping when the bandwidth is too broad, and this can be ameliorated using multi-scale inversion strategy, gradually increasing the frequency bandwidth (*Bunks et al., 1995*). Our FWI runs were performed from low to high frequency in two main steps: 6-8-10-15 Hz and 6-8-15-20 Hz. The time step is 0.712 ms and 0.437 ms for the two stage FWI runs respectively.

Ricker source wavelets with central frequency of 5 and 8 Hz ([Figure S3a](#)) were used for the two-step runs, respectively. For the 5 Hz and 8 Hz Ricker wavelet FWI runs, the

115 peak values of the wavelet are placed at 282 and 176 ms respectively, and the initial time
shift was calculated through cross-correlation between the synthetic data and real data. A
potential cause of error in our inversion is the source wavelet. As the seismic records are
a convolution of the source with the reflectivity series (the velocity model we seek to
obtain), errors in the source wavelet will map directly into errors in the final model.
120 However, it is rare in seismic experiments to measure the far-field response of the air gun
signature directly (e.g., *Ziolkowski, 1991*) nor have a robust estimate of the response of
the hydrophones. Previous studies have estimated source wavelet from seismic data (e.g.,
Collier & Singh, 1997; Arnulf et al., 2014; Harding et al., 2016; Skopintseva et al.,
2016), and here we also tried to extract the source wavelet from the data and compare the
125 results. Data-extracted source wavelets ([Figure S4](#)) were also tested for profile K1, and
the source wavelet was estimated from the direct arrivals of five near-offset traces from
each shot gather following the method of *Collier and Singh (1997)*, and then same
bandpass filtered as the dataset for FWI to make the source wavelet. The gradient of first
iteration of profile K1 was used to evaluate the differences using different source
130 wavelets, i.e. the extracted source wavelet and the Ricker wavelet used in the study.
There are subtle differences among the two gradients, but the general features remain the
same, and geological interpretation of FWI models obtained with either source wavelets
would not change ([Figure S5](#)).

We also tested a modified starting model in which all velocity values larger than 7.0
135 km/s are set to 7.0 km/s for profile K1 ([Figure S7](#)). This test shows that for profile K1
different starting models results in very similar structure in the upper ~2 km, with the
only notable discrepancy being a small feature ~1.5 km deep beneath the eastern flank of
the OCC near the termination. This test gives us confidence that our results in the upper
~2 km are robust and not significantly influenced by the unconstrained velocities >2 km
below seafloor in the starting models ([Figure S7](#)).

140 Convergence can be accelerated using appropriate gradient preconditioning. During
each stage, the gradient of the misfit function was pre-conditioned by allowing
perturbations to the gradient between 0.2 km below the seafloor and model base depth,
with a 0.2-km-long cosine tapering to the seafloor, and Gaussian smoothing the gradient
of 2 km × 0.5 km horizontally and vertically in the space domain. Checkerboard
145 resolution tests ([Figure S8](#)) indicate that, if the deep, long-wavelength velocity structure
were known, features that are ~0.5-km-wide and ~0.5-km-long could be trusted and
interpreted, except at the ends of profiles where data coverage is poor. The initial models
used for traveltimes tomography shown in [Figure S3b](#) indicate the starting models are not
well constrained deeper than 2 km below the seafloor, thus the FWI may resolve features
150 of that size (2 km × 0.5 km), but their absolute velocity value is not resolved. The
goodness of fit between the observed and the predicted waveforms is given by the
normalized misfit function ([Figure S9](#)). Inversion was terminated after the iteration at
which the misfit was not significantly reduced and the velocity structure did not show
much improvement.

155 Compared to the initial input traveltimes tomography models, the FWI models shows
large-scale similarity and clear refinement of the small-scale structures and deeper
illumination ([Figure S10](#)). The large lateral velocity variations in both strike and dip

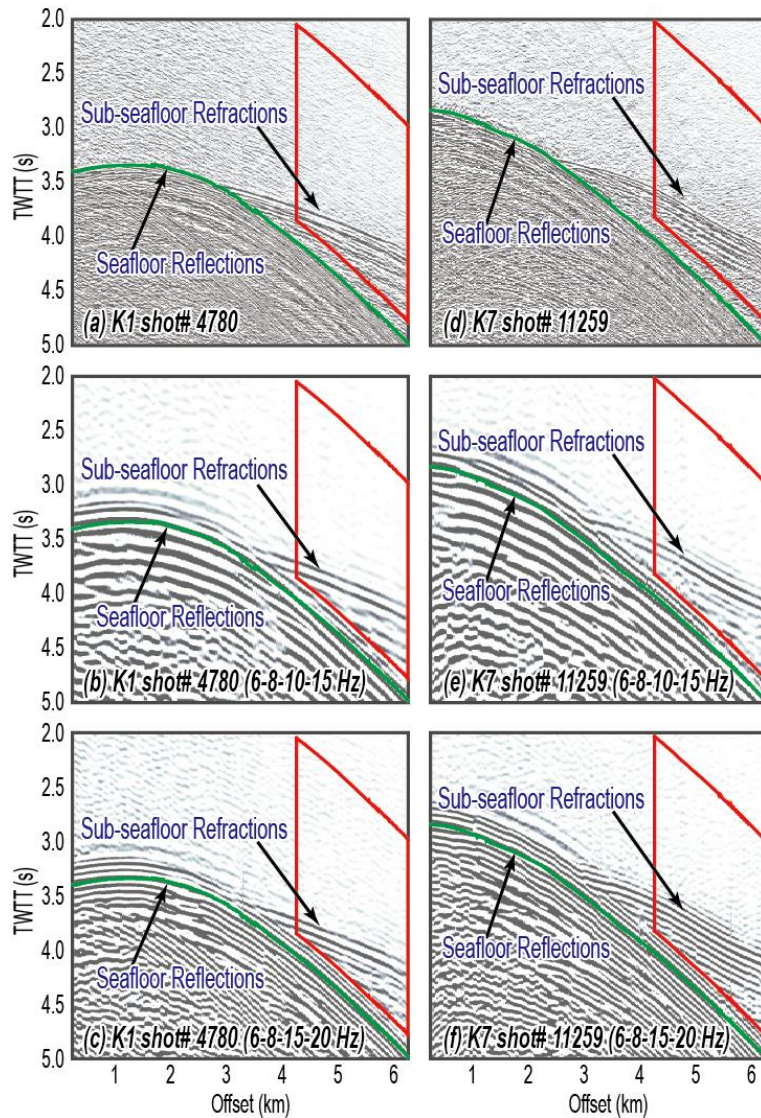
directions can be seen clearly by displaying the FWI models relative to the same initial 1-D model with seafloor velocity of 3.7 km s^{-1} and vertical velocity gradient of 1.75 s^{-1} (Figure S3b).

Text S3. Reverse time migration

RTM is a two-way wave equation migration technique commonly used for accurate imaging of subsurface complex structures (Baysal *et al.*, 1983). The imaging condition of RTM is estimated by cross-correlating the forward source wavefield and backward receiver wavefield in time. Compared to Kirchhoff and one-way wave equation based algorithms, RTM computes full two-way numerical solutions to the wave equation, thus it has no dip limitation and can handle extreme lateral velocity variations using all possible arrivals, promising better subsurface imaging.

RTM is closely related to full-wavefield inversion. The FWI can be thought of as an alternating sequence of migration and model updates (Mora, 1989). FWI migrates residual wavefields and calculates the gradient of the misfit function along which the perturbation model is searched by cross-correlating the forward source wavefield and the back-propagated residual wavefields, assuming that all propagation effects were corrected for and that the images are properly scaled. The perturbation model obtained after the first FWI iteration of the local optimization looks like a migrated image obtained by RTM. The difference is that the receiver wavefield is back propagated in RTM, whereas the residual wavefield is back propagated in FWI. The modeling scheme implemented within our RTM algorithm is the same as the one used for the FWI for consistency.

The artifacts of RTM occur when diving waves, head-waves or backscattered waves cross-correlate at the imaging step. These events are particularly strong where high velocity contrasts or high velocity gradient exists, and are most noticeable in the shallow section. To remove this artifact, preprocessing of the MCS data included a Butterworth bandpass filter with corner frequencies of 6 and 50 Hz to constrain the frequencies of the sea surface data to ones that satisfy the stability criterion of a 6.25 m finite-difference grid, and a dip filter to remove the rough seafloor diffractions. The shallow refractions do not correspond to a true reflection event and cannot be focused correctly by the RTM, thus the energy associated with shallow refractions and far-offset seafloor reflections were muted prior to migration to improve the RTM imaging (Figure S11). The RTM images (Figure S12) were used to investigate the structural variability within the Kane OCC.



195 **Figure S1.** Two representative shot gathers after LIFT processing from seismic profiles K1 and K7 over the Kane OCC. Horizontal axes are distances from source to receivers along the streamer, and vertical axes are two-way traveltime. (a, d) LIFT shot gather; (b, e) Bandpass filtered shot gather with 6-8-10-15 Hz; (c, f) Bandpass filtered shot gather with 6-8-15-20 Hz. Red trapezoids outline the data window used for FWI. Shot gather positions are shown in [Figure 1a](#) by red stars.

200

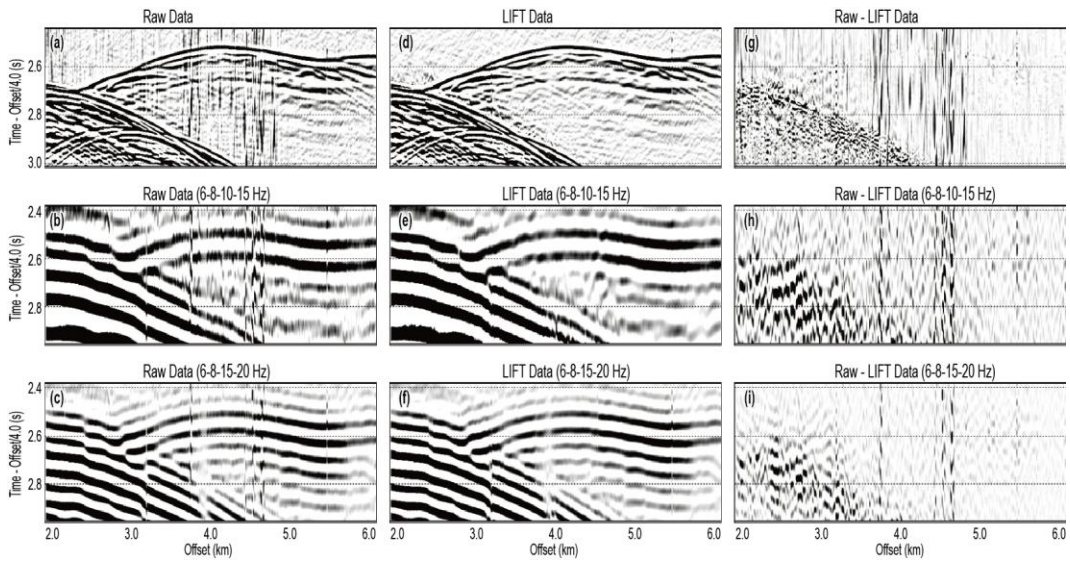


Figure S2. Comparison of the seismic data (shot# 11259 along profile K7) before and after LIFT processing. (a-c) Raw shot gather without filter, with bandpass filter 6-8-10-15 Hz, and 6-8-15-20 Hz respectively; (d-f) LIFT data; (g-h) Difference between the raw data and LIFT data.

205

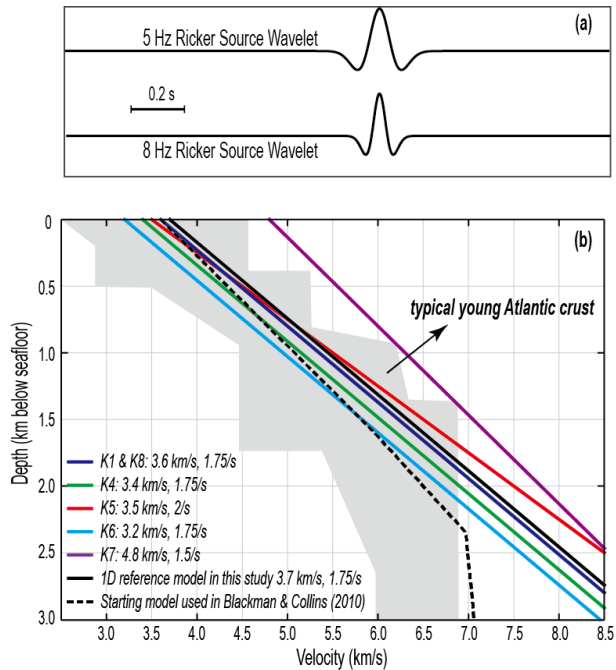
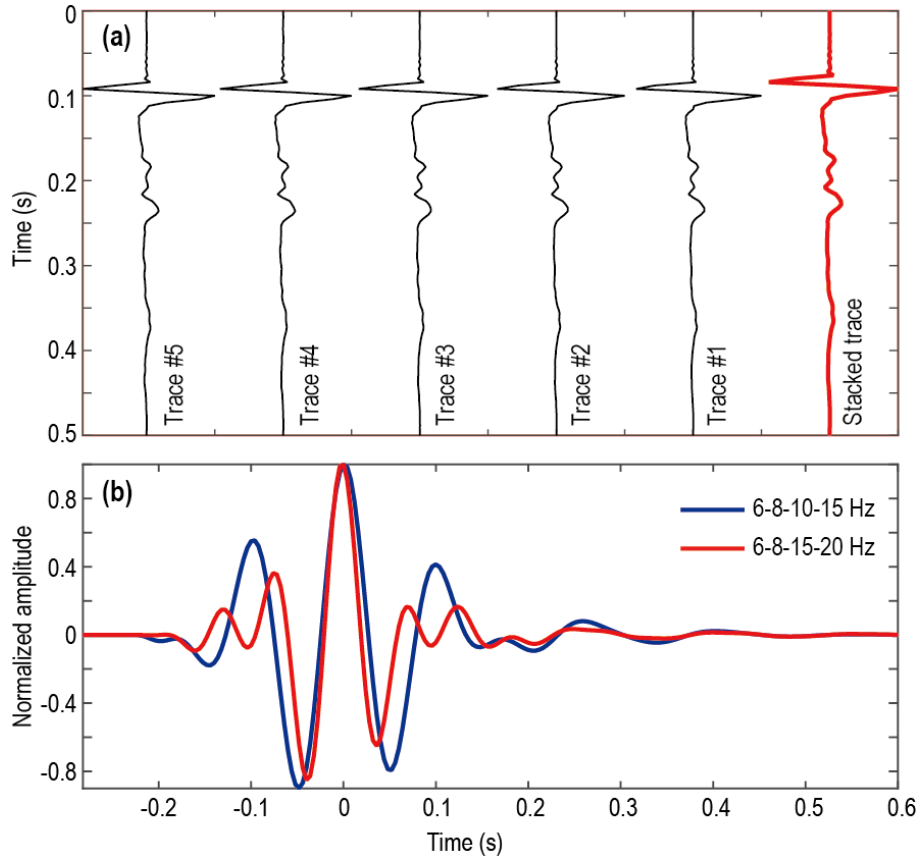
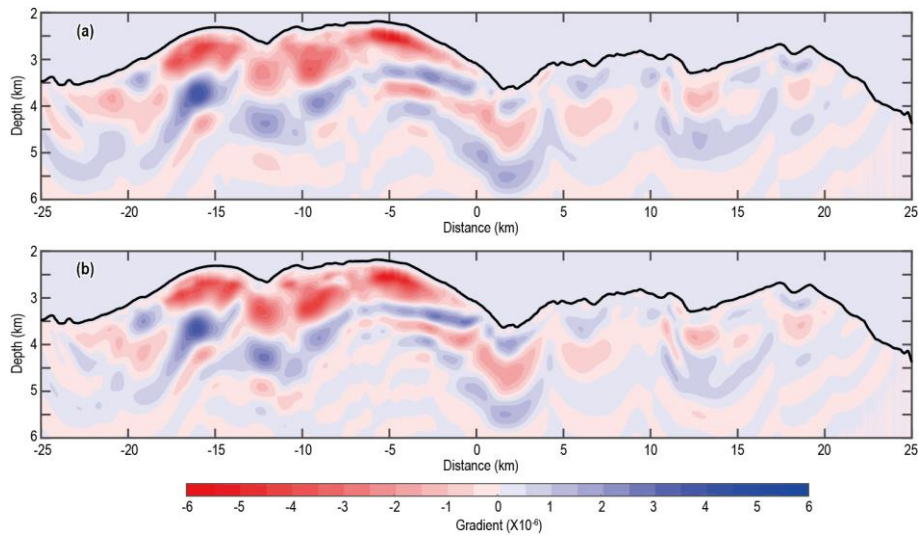


Figure S3. (a) Source wavelets used for full waveform inversion (FWI); (b) Starting models used for traveltime tomography of each seismic profile (Xu *et al.*, 2009), and average 1-D reference model used for displaying the velocity variations of all the six seismic profiles. Dashed line shows the starting model used in Blackman and Collins (2010) to map the structure of Atlantis Massif OCC. Shaded area marks the velocity-depth envelope of young Atlantic crust (White *et al.*, 1992).

210



215 **Figure S4.** Example of data-extracted source wavelet for profile K1 shot# 4780. (a) Five near-offset traces were stacked to form data-extracted source wavelet; (b) Estimated source wavelets with 6-8-10-15 Hz (blue) and 6-8-15-20 Hz (red) bandpass filters.



220 **Figure S5.** Comparison of velocity gradient calculated from the first iteration of profile K1. Calculated gradients were obtained using (a) 5 Hz Ricker source wavelet and (b) 6-8-10-15 Hz bandpass filtered data-extracted source wavelet.

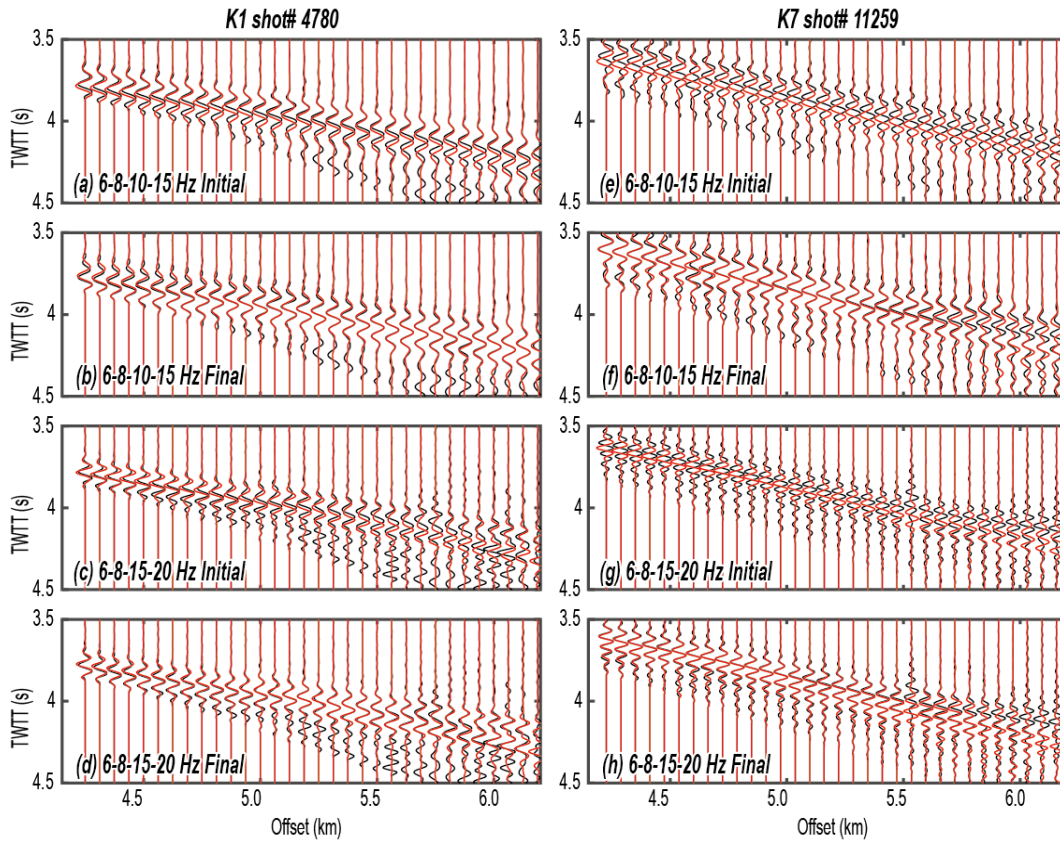
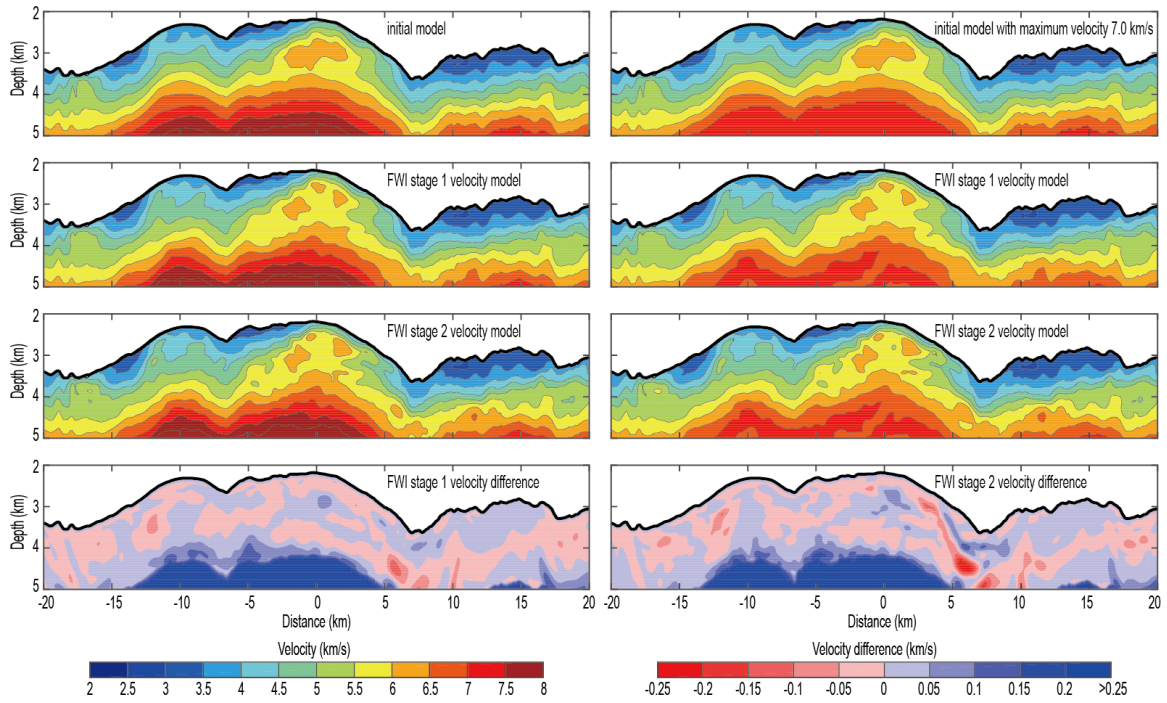
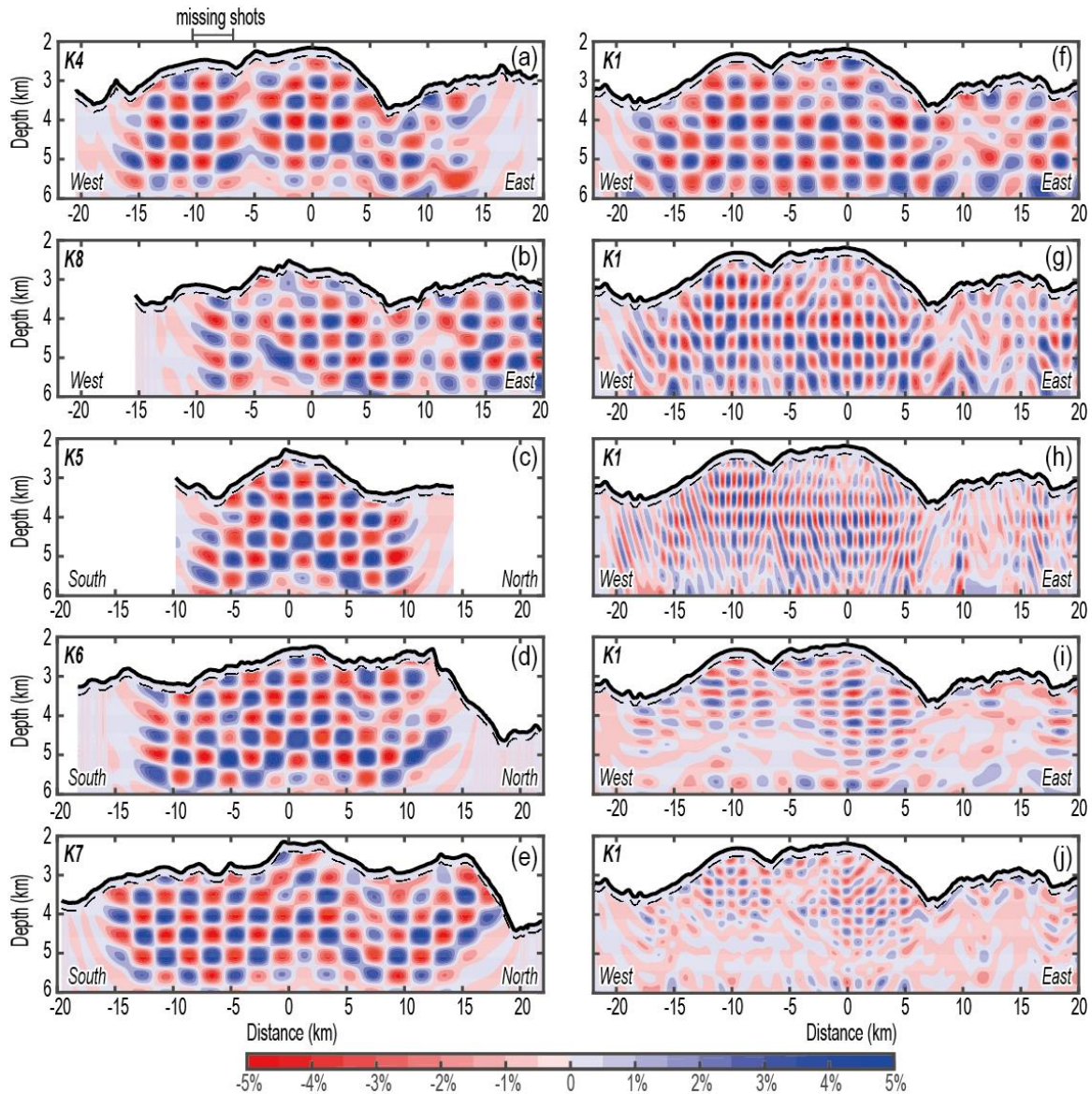


Figure S6. Comparison of observed data (in black) and synthetically calculated data (in red) before and after two-step FWI runs of the two representative shot gathers shown in [Figure S1](#). (a, e) Initial data fitting with 6-8-10-15 Hz bandpass filter; (b, f) Data fitting after first-step FWI run; (c, g) Initial data fitting with 6-8-15-20 Hz bandpass filter; (d, h) Final data fitting after second-step FWI run.

225



230 **Figure S7.** Comparison of FWI results of profile K1 with original initial model and modified initial model. The modified initial model was built by setting all velocity higher than 7.0 km/s to 7.0 km/s.



235 **Figure S8.** Results of checkerboard resolution tests for FWI. True anomaly pattern is created by a sine function with a maximum amplitude of $\pm 5\%$ of the FWI velocity model. Sizes of the checkerboard are 2.0-km-wide and 0.5-km-thick for the left panel (a-e) (K4, K8, K5, K6, K7), and (f) 2.0 km \times 0.5 km, (g) 1.0 km \times 0.5 km, (h) 0.5 km \times 0.5 km, (i) 2.0 km \times 0.25 km, (j) 1.0 km \times 0.25 km for the right panel (K1) from top to bottom. The dashed lines indicate 200 m below seafloor for shallow subsurface tapering.

240

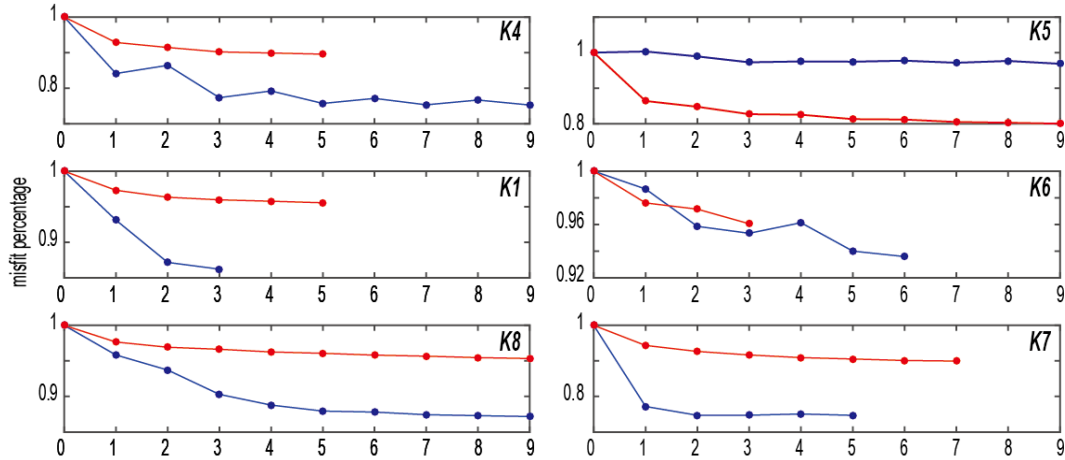


Figure S9. Normalized misfit function for each iteration shown in percentage with respect to the initial misfit. The normalized misfit functions of the first (6-8-10-15 Hz) and second (6-8-15-20 Hz) stage FWI run are indicated by blue and red dots respectively. FWI run was terminated after the iteration at which the misfit was not significantly reduced.

245

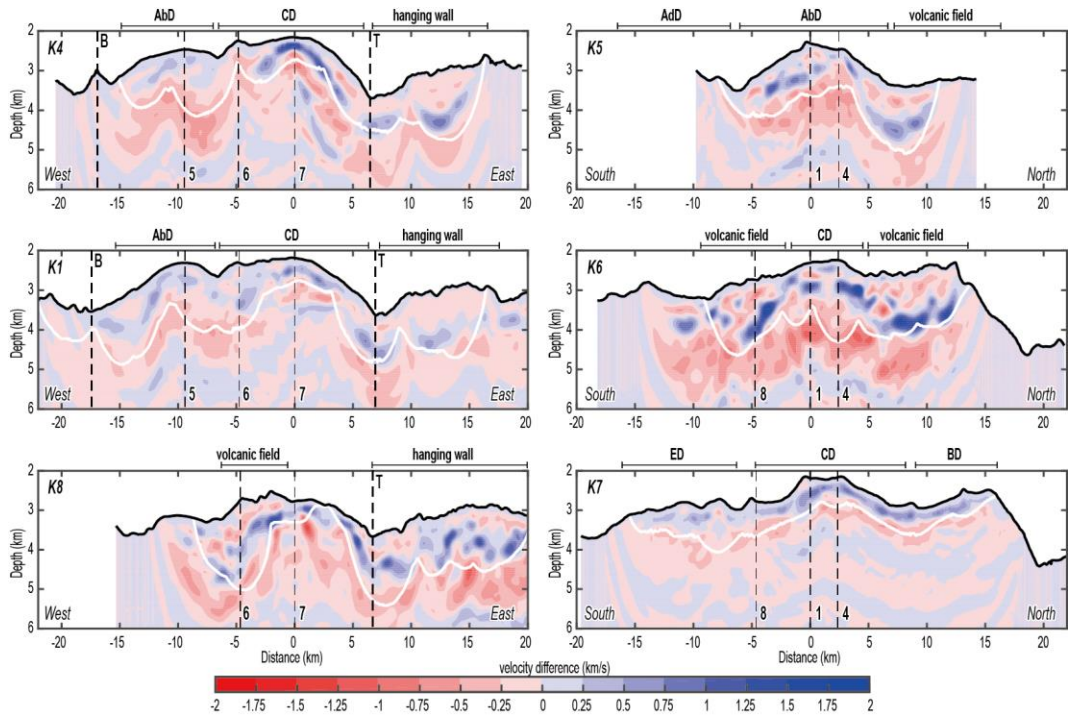
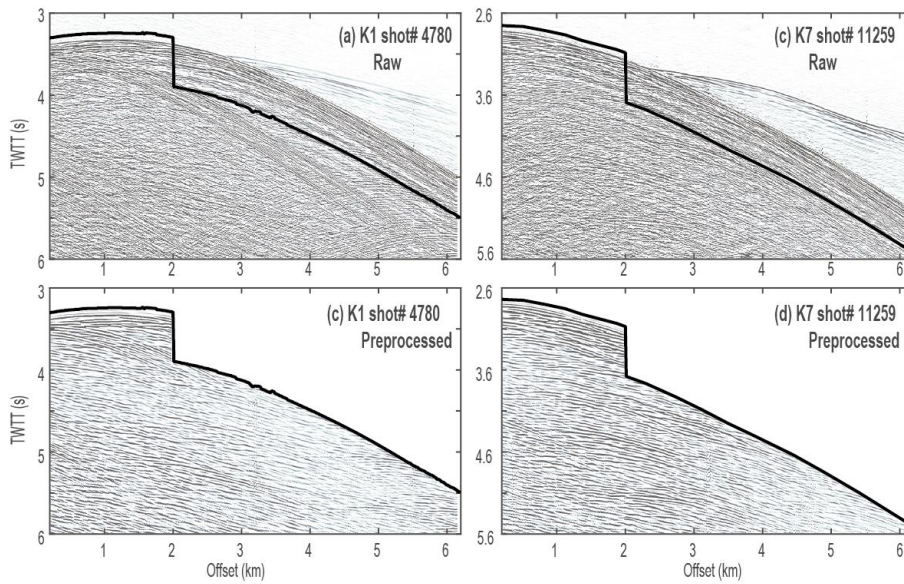
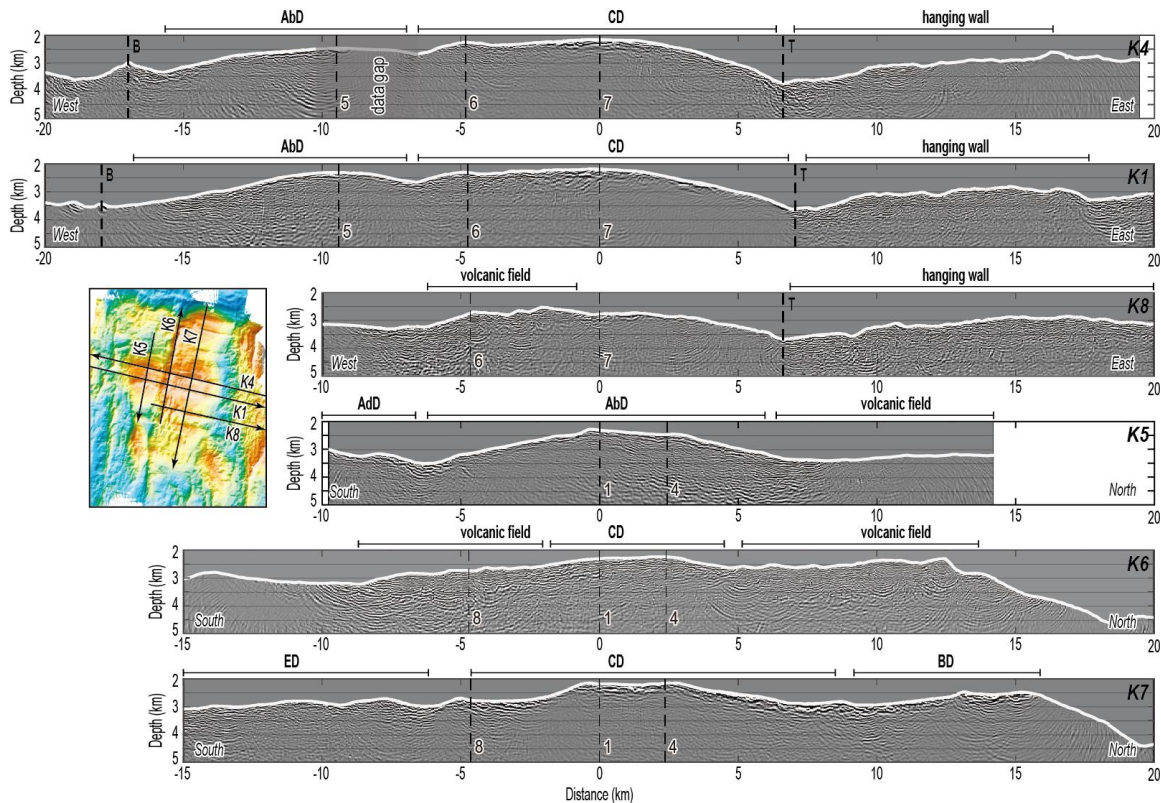


Figure S10. FWI updates with respect to initial traveltome tomography models. FWI models show clear improvement in the small-scale structures and deeper illumination. The limit of the ray coverage for the traveltome tomography inversion is indicated by a white line.

250



255 **Figure S11.** Two representative shot gathers from seismic profiles K1 and K7 over the Kane oceanic core complex. Horizontal axes are distances from source to receivers along the streamer, and vertical axes are two-way traveltime. The thick black lines show the mute window. (a, c) Raw shot gather; (b, d) Preprocessed gather for RTM. The energy associated with shallow refractions and far-offset seafloor reflections were muted prior to migration to improve the RTM imaging.



260 **Figure S12.** The RTM images derived from migrating preprocessed MCS shot gathers
 (Figure S11) based on high-fidelity FWI models (Figure 2). Profile locations are shown
 in the inset. Morphological features are labeled at the top of the profiles. Thick dashed
 lines indicate locations of breakaway (B) and termination (T). Thin dashed lines show
 crossings between dip and strike profiles.

265

References

- Aghaei, O., Nedimović, M. R., Carton, H., Carbotte, S. M., Canales, J. P., & Mutter, J. C. (2014),
 Crustal thickness and Moho character of the fast-spreading East Pacific Rise from 9°42'N to
 9°57'N from poststack-migrated 3D MCS data. *Geochemistry, Geophysics, Geosystems*,
 270 *15*(3), 634-657. <https://doi.org/10.1002/2013GC005069>.
- Arnulf, A. F., Harding, A. J., Singh, S. C., Kent, G. M., & Crawford, W. C. (2014). Nature of
 upper crust beneath the lucky strike volcano using elastic full waveform inversion of
 streamer data. *Geophysical Journal International*, *196*, 1471-1491.
<https://doi.org/10.1093/gji/ggt461>.
- 275 Barzilai, J., & Borwein, J. (1988). Two point step size gradient methods. *IMA Journal of
 Numerical Analysis*, *8*(1), 141-148. <https://doi.org/10.1093/imanum/8.1.141>.
- Baysal, E., Kosloff, D. D., & Sherwood, J. W. C. (1983). Reverse time migration. *Geophysics*,
48(11), 1514-1524. <https://doi.org/10.1190/1.1441434>.

- 280 Blackman, D. K., & Collins, J. A. (2010). Lower crustal variability and the crust/mantle transition at the Atlantis Massif oceanic core complex. *Geophysical Research Letters*, 37(24), 701-719. <https://doi.org/10.1029/2010GL045165>.
- Bunks, C., Saleck, F., Zaleski, S., & Chavent, G. (1995). Multiscale seismic waveform inversion. *Geophysics*, 60(5), 1457-1473. <https://doi.org/10.1190/1.1443880>.
- 285 Choo, J., Downton, J., & Dewar, J. (2004). LIFT: A new and practical approach to noise and multiple attenuation. *First Break*, 22(5), 39-44. <https://doi.org/10.3997/1365-2397.2004009>.
- Clairbout, J. (1971). Toward a unified theory of reflector mapping. *Geophysics*, 36(3), 467-481. <https://doi.org/10.1190/1.1440185>.
- 290 Collier, J. S., & Singh, S. C. (1997). Detailed structure of the top of the melt body beneath the East Pacific Rise at 9°40'N from waveform inversion of seismic reflection data, *Journal of Geophysical Research*, 102(B9), 20,287-20,304. <https://doi.org/10.1029/97JB01514>.
- Grippo, L., & Lucidi, S. (1997). A globally convergent version of the polak-ribière conjugate gradient method. *Mathematical Programming*, 78(3), 375-391. <https://doi.org/10.1007/BF02614362>.
- 295 Han, S., Carbotte, S. M., Canales, J. P., Carton, H., Nedimović, M. R., Gibson, J., & Horning, G. (2016). Seismic reflection imaging of the Juan de Fuca plate from ridge to trench: new constraints on the distribution of faulting and evolution of the crust prior to subduction. *Journal of Geophysical Research*, 121(3), 1849-1872. <https://doi.org/10.1002/2015JB012416>.
- 300 Harding, A. J., Arnulf, A. F., & Blackman, D. K. (2016). Velocity structure near IODP Hole U1309D, Atlantis Massif, from waveform inversion of streamer data and borehole measurements, *Geochemistry, Geophysics, Geosystems*, 17, 1990-2014. <https://doi.org/10.1002/2016GC006312>.
- 305 Lailly, P. (1983). The seismic inverse problem as a sequence of before stack migrations. In J. Bednar, E. Robinson, A. Weglein (Eds.), *Conference on Inverse Scattering, Theory and Applications* (pp. 206-210), Society for Industrial and Applied Mathematics.
- Levander, A. R. (1988). Fourth-order finite-difference P-SV seismograms. *Geophysics*, 53(11), 1425-1436, <https://doi.org/10.1190/1.1442422>.
- Mora, P. (1989). Inversion = migration + tomography. *Geophysics*, 54(12), 1575-1586. <https://doi.org/10.1190/1.1442625>.
- 310 Operto, S., Virieux J., Amestoy P., L'Excellent J., Giraud L., & Ali H. (2007). 3D finite-difference frequency-domain modeling of viscoacoustic wave propagation using a massively parallel direct solver: A feasibility study. *Geophysics*, 72(1), 2265-2269. <https://doi.org/10.1190/1.2369987>.
- 315 Pratt, R. G. (1999). Seismic waveform inversion in the frequency domain. Part I: Theory and verification in a physical scale model. *Geophysics*, 64(3), 888-901. <https://doi.org/10.1190/1.1444597>.
- Sirgue, L., & Pratt R. (2004). Efficient waveform inversion and imaging: A strategy for selecting temporal frequencies. *Geophysics*, 69(1), 231-248. <https://doi.org/10.1190/1.1649391>.

- 320 Skopintseva, L. V., Maaø, F. A., & Pedersen., Ø. (2016). Importance of the Source Estimation in
FWI - Sensitivity and Examples. *Eage Conference & Exhibition*.
<https://doi.org/10.3997/2214-4609.201601015>.
- Tarantola, A. (1984). Inversion of seismic reflection data in the acoustic approximation.
Geophysics, 49(8), 1259-1266. <https://doi.org/10.1190/1.1441754>.
- 325 Vigh, D., & Starr, E. (2008). 3D prestack plane-wave, full-waveform inversion. *Geophysics*,
73(5), VE135. <https://doi.org/10.1190/1.2952623>.
- White, R. S., McKenzie, D., & O'Nions, R. K. (1992), Oceanic crustal thickness from seismic
measurements and rare earth element inversions. *Journal of Geophysical Research*, 97,
19,683-19,715. <https://doi.org/10.1029/92JB01749>.
- 330 Xu, M., Canales, J. P., Tucholke, B. E., & Dubois, D. L. (2009). Heterogeneous seismic velocity
structure of the upper lithosphere at Kane oceanic core complex, Mid-Atlantic Ridge.
Geochemistry, Geophysics, Geosystems, 10(10), Q10001.
<https://doi.org/10.1029/2009GC002586>.
- Ziolkowski, A. (1991). Why don't we measure seismic signatures? *Geophysics*, 56(2), 190-201.
<https://doi.org/10.1190/1.1443031>.